Ceramics International 49 (2023) 18896–18905

Contents lists available at ScienceDirect

Ceramics International

journal homepage: www.elsevier.com/locate/ceramint

# Dysprosium doped calcium tungstate as an efficient electrode material for the electrochemical energy storage devices

Hafiz Talha Hasnain Rana [a], Naveed Akhtar Shad [b], S. Hussain [c], Asim Jilani [d], Muhammad Umair [a], Muhammad Munir Sajid [e], Muhammad Faheem [c], Attaullah Shah [f], Yasir Jamil [a], Munib Ahmed Shafique [g], Yasir Javed [a,*]

[a] Department of Physics, University of Agriculture, Faisalabad, Pakistan
[b] National Institute for Biotechnology and Genetic Engineering, Jhang Road, Faisalabad, Pakistan
[c] Department of Physics, Division of Science and Technology, University of Education Lahore, Pakistan
[d] Center of Nanotechnology, King Abdul-Aziz University, Jeddah, 21589, Saudi Arabia
[e] Henan Key Laboratory of Photovoltaic Materials, School of Physics, Henan Normal University, Xinxiang, 453007, China
[f] National Institute of Lasers and Optronics College, Pakistan Institute of Engineering and Applied Sciences, Nilore, Islamabad, 45650, Pakistan
[g] Central Analytical Facility Division, Pakistan Institute of Nuclear Science and Technology, Pinstech, Islamabad, Pakistan

ARTICLE INFO

Handling Editor: Dr P. Vincenzini

*Keywords:*
Dysprosium
Calcium tungstate
Electrochemical properties
Diffusion-controlled mechanism

ABSTRACT

Tungstate-based nanostructures improve electrochemical performance and offer many advantages due to their charge transport capabilities, excellent corrosion resistance, and superior optical and electrical characteristics. The main purpose of this study is to synthesize the calcium tungstate and dysprosium (Dy) doped calcium tungstate nanomaterials by using the hydrothermal method and investigate the effect of Dy doping on the electrochemical properties of calcium tungstate nanomaterials. The Dy doping changes the structural properties of materials such as a decrease in crystallite size, change in lattice parameters, and volume of the unit cell. The band gap of $CaWO_4$ reduces from 3.32 eV to 3.06 eV with increasing Dy concentration. SEM images reveal the spherical shape of the $CaWO_4$ and Dy (0.8%) doped $CaWO_4$ nanomaterials. The electrochemical properties show that Dy doping enhances the performance of $CaWO_4$ nanomaterials as a supercapacitor. The specific capacity increases to 624 C/g with 0.8% Dy doping in $CaWO_4$ as compared to 115 C/g of undoped $CaWO_4$ at a sweep rate of 5 mV/s. The theoretical evaluation shows that the diffusion-controlled mechanism dominates with the increasing sweep rate which presents the potential of Dy (0.8%) doped $CaWO_4$ for supercapattery-based hybrid devices.

## 1. Introduction

Non-renewable energy sources are depleting as an outcome of economic growth [1] along with additional issues related to the usage of fuels including high cost, toxicity, and global warming [2]. To overcome the erratic nature of renewable sources of energy and boost the amount of electricity delivered to the grid, energy storage systems (ESS) are essential. The two essential areas of technology for energy storage that drew the most interest are supercapacitors and batteries. Supercapacitors are recognized for their high specific power, whereas batteries are distinguished by their high specific energy values [3,4]. Supercapacitors have been the subject of extensive study to meet the energy needs of the present and the future. Supercapacitors offer high power capacities, rapid rates of charging/discharging, longer life-cycle, and environmentally friendly designs that might replace or work with batteries [5,6]. This has made it possible to create more sophisticated hybrid ESS for both stationary and onboard applications [2]. Supercapacitors can be used in hybrid electric automobiles since they charge quickly. This technology can be used in the fields of aircraft, industry, road transportation, and flexible/wearable electronics. Supercapacitors fall into two categories: pseudo capacitors which store energy by redox processes, and electric double-layer capacitors, where energy is stored electrostatically. Typically, the hybrid ESS store energy using electrochemical and electrostatic processes simultaneously. In every device for energy storage, the electrode material is the most important part. The supercapacitor's charging/discharging efficiency is significantly aided

* Corresponding author.
*E-mail address:* myasi60@hotmail.com (Y. Javed).

https://doi.org/10.1016/j.ceramint.2023.03.013
Received 23 November 2022; Received in revised form 1 March 2023; Accepted 2 March 2023
Available online 3 March 2023

by the electrode material [1,7,8]. Graphene, fluorene, and other carbon derivatives serve as the typical electrode material, separated by an inert porous sheet [9]. Theoretical models predict that better optical and electrical features of tungstate-based nanostructures can improve electrochemical performance [10,11].

Calcium tungstate ($CaWO_4$) can be a potential material for energy storage applications due to its unique properties such as excellent mechanical strength, binary transition state, high oxide ion conductivity, oxidation states, and favorable thermal and chemical stabilities [12]. $CaWO_4$ has received a great deal of attention over the past century because of its intriguing luminescence and structural characteristics [13–16]. $CaWO_4$ can be regarded as a useful material that contains $Ca^{2+}$ ions and $WO_4^{2-}$ groups with a coordination number of eight for $Ca^{2+}$ and four for $W^{6+}$ [17]. $CaWO_4$ emits a sky-blue glow when exposed to shortwave ultraviolet light [18]. $CaWO_4$ crystallizes into bipyramidal pseudo-octahedra and belongs to the tetragonal crystal system. $CaWO_4$ nanomaterials have been reported for several applications such as optical characteristics [19], photocatalysis [20], and laser [21].

Dy-doped nanomaterials have presented potential in applications such as photocatalytic degradation [22,23], sensor [24], supercapacitors [25], batteries [26], light emitting diode [27,28], and data-storage applications like hard drives since these are particularly susceptible to magnetization. Dy doping is also reported in different materials which increases the electrochemical performance of the host material manifold. Aghazadeh and Ganjali (2018) reported that Dy-doped $Fe_3O_4$ nanoparticles (NPs) for anode materials with a 93.9% capacitive retention rate for use in supercapacitors [29]. Bagwade et al. (2021) highlighted the $Dy_2S_3$ composite for the asymmetric supercapacitors with 86% stability for 5000 cycles, and 82% flexibility at a bending angle of 165° [9]. Deepti Gangwar et al. (2019) observed an increase in capacitance with the rise in Dy concentrations in manganese oxide. The capacitance increased by two times for (15 mol%) Dy doped as compared to undoped α-$MnO_2$ [30]. Raja et al. (2021) reported synergic properties and improved capacitance performance up to 752 $Fg^{-1}$ at 1 $Ag^{-1}$ current density by redox additive-based $Dy_2WO_6$–ZnO composite electrodes, which also provided cycling stability of 89% up to 2000 cycles [25]. Alhashmialameer et al. synthesized Dy (0.05 M) doped $NiMnO_3$ nanoflakes by hydrothermal method and observed specific capacitance and energy density of 2006 F/g and 72.35 W/kg respectively. The higher electrochemical response of the materials was attributed to the higher ionic charge of Dy species as compare to Ni and Mn [31]. These studies have shown that Dy can be useful for electrode material in next generation energy storage devices [24,32]. However, reports on $CaWO_4$ for supercapacitor application are very rare. In the current study, a hydrothermal method has been used to synthesize $CaWO_4$ and Dy-doped $CaWO_4$ nanomaterials and probe their potential as a working electrode for the supercapacitor. The synthesized materials have been characterized by XRD, SEM, EDS, XPS, UV–Vis spectroscopy, and FTIR spectroscopy. Then $CaWO_4$ and Dy (0.8%) doped $CaWO_4$ nanomaterials are evaluated as potential electrode materials for supercapacitors.

## 2. Experimental section

### 2.1. Chemicals

Calcium chloride dihydrate ($CaCl_2.2H_2O$, SIGMA-ALDRICH, 99%), sodium tungstate dihydrate ($NaWO4{\cdot}2H_2O$, DAEJUNG, 98%), dysprosium (III) nitrate pentahydrate [Dy $(NO_3)_3{\cdot}5H_2O$, Alfa Aesar, 99.9%], and Polyethylene glycol [$H(CH_2CH_2O)_nOH$, DAEJUNG]. All the materials were used without any further purification.

### 2.2. Preparation of materials

In a typical synthesis, 0.25 M $Na_2WO_4$. $2H_2O$ (sodium tungstate dihydrate) was added to 100 ml of distilled water, and the solution was stirred for 20 min. The 0.5 M solution of $CaCl_2$. $2H_2O$ (calcium chloride dihydrate) was prepared separately. The two solutions were mixed by adding sodium tungstate solution dropwise. The PEG (0.2 g) was introduced into the solution as a surfactant. The prepared mixture was put into a Teflon-lined autoclave to undergo a 15 h hydrothermal treatment at 200 °C. The attained precipitates were centrifuged and washed three times with distilled water, then dried overnight in a vacuum oven at 60 °C. The dried product was ground with a pestle and mortar to obtain the $CaWO_4$ nanomaterials. The Dy-doped $CaWO_4$ nanomaterials were prepared by adding dysprosium (III) nitrate pentahydrate with the concentration of 0.4%, 0.6%, and 0.8% and following the above procedure. The obtained products were elaborately characterized using state-of-the-art facilities.

### 2.3. Characterization tools

The X-ray diffraction investigation performed using an X-ray diffractometer (Bruker D2 Phaser) with a Cu-Kα beam (λ = 0.15406 nm) showed the crystalline nature of synthesized nanomaterials. The morphology of prepared nanomaterials was examined by employing the Nova Nano SEM. Using a (Cary-630) FTIR spectrophotometer, Fourier transforms infrared spectroscopy was performed for the identification of functional groups of the nanomaterials. The optical characteristics of prepared nanomaterials were evaluated by employing a UV–Vis spectrometer (T80). Surface and functional analysis were performed by Raman spectroscopy and X-ray photoelectron spectroscopy (PHI-Versa Prob II, PHI, Chanhassen, MN, USA) under a high vacuum ($10^{-7}$ Pa). Atomic resolution TEM -200F with 2 CS correctors, attached with Gatan software was used for structural analysis. The elemental analysis is further done by ICP-OES (Model: iCAP 6500, Thermo Scientific UK) at RF power of 1150 Watt.

### 2.4. Electrochemical studies

The electrochemical behavior of calcium tungstate and dysprosium (0.8%) doped calcium tungstate electrodes were analyzed by CV, GCD, and EIS in a 2 M KOH solution (electrolyte) using CS310 Electrochemical workstation. Three electrode systems were used: the nanomaterials-modified Ni foam served as the working electrode, the Pt wire worked as a counter electrode, and the Ag/AgCl electrode was used as a reference electrode. The graphite, PVA (Polyvinyl Alcohol), and synthesized nanomaterials with a mass ratio (1:1:8) respectively were used to manufacture the working electrode. The prepared paste was coated on 1 × 1 $cm^2$ nickel foam and then dried in air at 90 °C for 20 min.

## 3. Results and discussion

### 3.1. Characterization of materials

The structural and phase information of calcium tungstate nanomaterials are determined by XRD analysis as shown in Fig. 1.The diffraction peaks are appeared at 2θ values of 29.03°, 34.42°, 39.45°, 43.56°, 45.71°, 47.37°, 49.36°, 53.35°, 54.56°, 56.54°, 58.15°, and 59.73° matched with calcium tungstate [33], JCPDS card number 01-077-2234 and depicts the tetragonal phase [34]. The XRD patterns of Dy-doped $CaWO_4$ present a slight shift in peaks towards lower 2θ values. The peak shifting increases as the Dy concentration rises. This transfer may be associated with the difference in ionic radii of dopant and host atoms (Dy = 116.7 p.m. and Ca = 114 p.m.), consequently inducing micro-strain in the lattice [35]. We also observe that certain peaks vanish with the increase in Dy doping which indicates effective dispersion of Dy ions in the host lattice [36]. Using Scherrer's formula, crystallite size is calculated and it is observed that crystallite size decreases from 21 nm to 14 nm after doping, also evident with peak broadening with rising Dy doping level. The calculated lattice cell parameters of $CaWO_4$ and Dy-doped $CaWO_4$ are provided in Table 1 along with

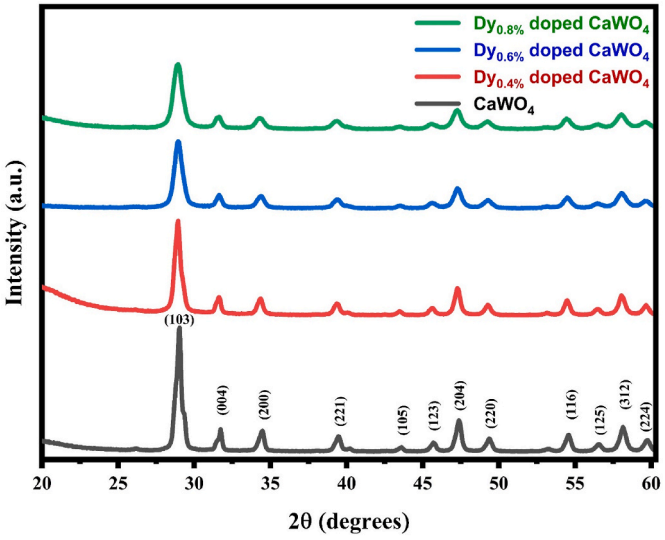


**Fig. 1.** XRD patterns of synthesized $CaWO_4$ and Dy (0.4%, 0.6%, 0.8%) doped $CaWO_4$ nanostructures in the 2 thetas range from 20° to 60°.

**Table 1**
Comparison of the lattice constant, crystallite size, and volume of doped and undoped $CaWO_4$.

| Concentrations (x) | Lattice Constant (Å) | | Crystallite Size (nm) | Volume ($Å^3$) |
|---|---|---|---|---|
| | a | | c | |
| **JCPDS value** | 5.21 | | 11.31 | |
| $CaWO_4$ | 5.22 | | 11.29 | 21 | 307.63 |
| Dy (0.4%) doped $CaWO_4$ | 5.22 | | 11.31 | 19 | 308.17 |
| Dy (0.6%) doped $CaWO_4$ | 5.20 | | 11.35 | 15 | 306.904 |
| Dy (0.8%) doped $CaWO_4$ | 5.23 | | 11.32 | 14 | 309.63 |

standard values obtained from the JCPDS card. The values of lattice constants vary with the addition of Dy atoms due to the change in ionic radii as discussed above [37].

Fig. 2a represents the FTIR spectrum of different as-synthesized $CaWO_4$-based nanomaterials. In the FTIR spectrum, the bands found at 1644 $cm^{-1}$ and 922 $cm^{-1}$ are related to Dy–O and Ca–O bonding respectively [33,38,39]. The band at 1644 $cm^{-1}$ also indicate the wate molecules adsorbed on the surface of the nanomaterials [40,41]. The transmittance band at 766 $cm^{-1}$ belongs to $(WO_4)^{-2}$ [33]. The presence of different inorganic bands confirms the formation of $CaWO_4$ and the presence of dopant in the host lattice. The UV–Vis absorption spectrum is used to study the optical properties of the synthesized Dy-doped $CaWO_4$ nanomaterials. The bandgap and the type of electronic transitions can be determined from the absorption spectrum. When a semiconductor absorbs photons of energy larger than the bandgap of the semiconductor, an electron is transferred from the valence band to the conduction band, there occurs an abrupt increase in the absorbance of the material to the wavelength corresponding to the bandgap energy [42]. In Fig. 2b, the absorbance curves of $CaWO_4$, Dy (0.4%) doped $CaWO_4$, Dy (0.6%) doped $CaWO_4$, and Dy (0.8%) doped $CaWO_4$ show a peak at 262 nm, 241 nm, 245 nm, and 251 nm respectively [43]. The band gap is determined using Tauc plot method. Fig. 2c shows band gap curves for different materials. The undoped $CaWO_4$ has a band gap of 3.32 eV [18], whereas rising Dy concentration reduces the band i.e. 3.11 eV, 3.08 eV, and 3.06 eV respectively. According to the quantum size effect, the smaller the size of the NPs, the wider the energy bandgap. However, the decrease in energy bandgap for doped materials with Dy concentrations from 0.4% to 0.8% indicates that several structural defects are generating allowed states between the valence and conduction band [44].

SEM is used to examine the grain size and morphology of the nanomaterials. In Fig. 3 (a-b & d-e), the presence of nanosized particles is witnessed in both materials [45]. The spherical grains can be seen in the SEM images of $CaWO_4$ and Dy (0.8%) doped $CaWO_4$ nanomaterials. The average grain sizes of $CaWO_4$ and Dy (0.8%) doped $CaWO_4$ are 88.1 ± 21.4 nm and 28.5 ± 7.1 nm respectively, as deduced from the statistical histograms (Fig. 3c and f). The higher values of grain size than crystallite size indicate that grains are composed of more than one crystal. The polydispersity index of $CaWO_4$ and Dy (0.8%) doped $CaWO_4$ are 0.05 and 0.06 respectively and exhibit monodisperse size distributions. Fig. 3g shows the X-ray energy dispersive (EDS) spectrum of Dy (0.8%) doped $CaWO_4$ nanomaterials and indicates the presence of Dy, Ca, W and O. The EDS spectrum confirms the doping of Dy metal in the $CaWO_4$ and also chemical purity of the material. The atomic percentages of Dy, Ca, W, and O are 0.7%, 12.48%, 14.43%, and 72.39% respectively in the Dy (0.8%) doped $CaWO_4$. The ICP-OES is trace element detection technique which uses emission spectra to identify and quantify element present in the sample. The Dy concentration of 1.14% is observed in doped $CaWO_4$ sample. The difference in Dy concentration in two techniques i.e. EDX and ICP may be linked with the reason that EDX is usually provided chemical information of a specific portion of the sample, consequently.

The morphology of Dy (0.8%) doped CaWO4 NPs is further studied by using transmission electron microscopy (Fig. 4a-c). The low magnification bright field image shows spherical shape of the particles as observed in the case of SEM analysis. The sizes measured on different NPs also show the consistency with size distribution histograms determined from SEM images (Fig. 4a). The high-resolution images present high crystallinity of the NPs whereas fringe spacing of 0.412 nm (Fig. 4b) and 0.389 nm (Fig. 4c) represent (101) and (112) planes respectively. However, these d spacing values vary as compare to JCPDS card (01-077-2234) as discussed in the XRD results. This variation in interplanar distance can be linked with the incorporation Dy ions in the $CaWO_4$ lattice.

The surface states and chemical composition of Dy (0.8%) doped $CaWO_4$ nanomaterials are further investigated by X-ray photoelectron spectroscopy (XPS). Fig. 5a shows the XPS survey spectrum of Dy (0.8%) doped $CaWO_4$. The presence of different elements i.e. Dy, Ca, W, and O, is evidenced in the survey spectrum. To determine surface states, high-resolution XPS spectrums are recorded for all the elements (Fig. 5b-e). The structure of Dy 4d is more complicated than the basic doublet usually predicted due to spin-orbit splitting, however, due to identical primary quantum numbers of the two shells in this instance divided into four parts at 151.3 eV, 153.4 eV, 165.4 eV, and 167.7 eV [46]. In the case of Dy 4d, two peaks are observed at 151.3 eV and 153.4 eV which correspond to Dy 4d and $4d_{5/2}$ respectively [47]. The additional peaks are present at 165.4 eV and 167.7 eV which represent Dy $4d_{3/2}$ satellites (Fig. 5b). The Ca spectrum has peaks at binding energies of 344 eV, 347 eV, and 350.4 eV and indicate Ca 2p, $2p_{3/2}$, and 2p states respectively (Fig. 5c) [48,49]. The Auger peaks are evident in Fig. 5d at 30 eV and 31.82 eV [50], which equate to the metallic state of W along with peaks at binding energies of 34.02 eV and 36.22 eV indicating the $6^+$ oxidation state of W [3]. The binding energies of oxygen vacancies are located at 528.2 eV and 532.2 eV, where, 528.2 eV and 532.2 eV indicate the $O_1$ and $O_2$ respectively. The $O_1$ indicates the lattice oxygen and $O_2$ is related to OH on the surface (Fig. 5e) [51].

### 3.2. Electrochemical analysis

Cyclic voltammetry (CV) is an excellent and potent analytical tool for evaluating chemical responses incorporating an electron transfer [52]. CV analyzes the electrochemical characteristics and charge storage mechanism of calcium tungstate and dysprosium (0.8%) doped calcium

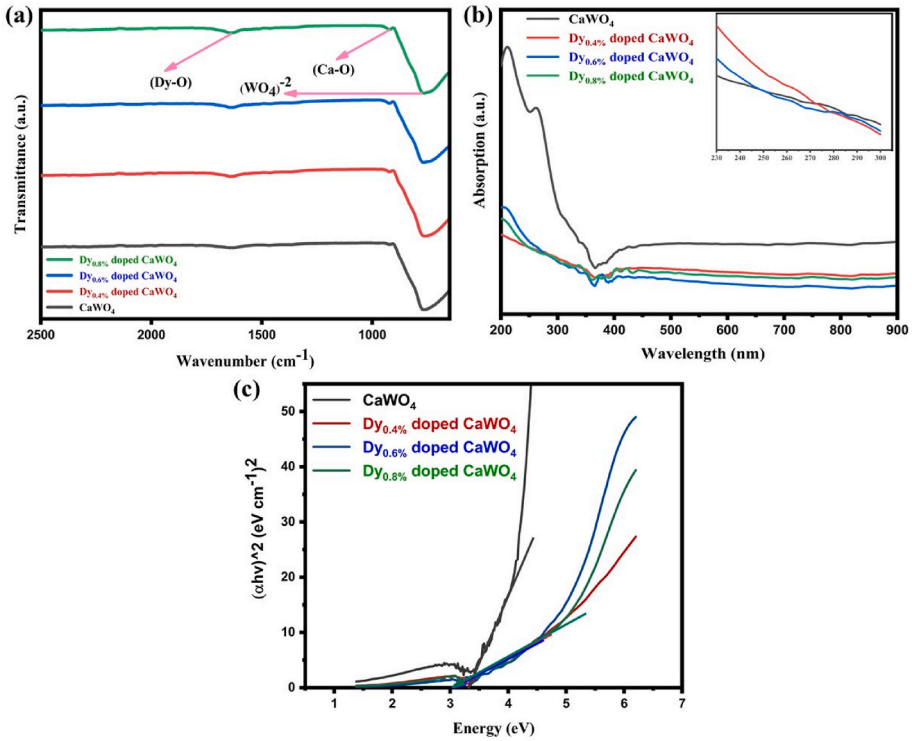


**Fig. 2.** (a) FTIR spectrums of $CaWO_4$ and Dy-doped $CaWO_4$ nanomaterials, (b) UV–Vis absorption spectrums of synthesized materials, (c) Tauc's plots used for the determination of energy band gaps.

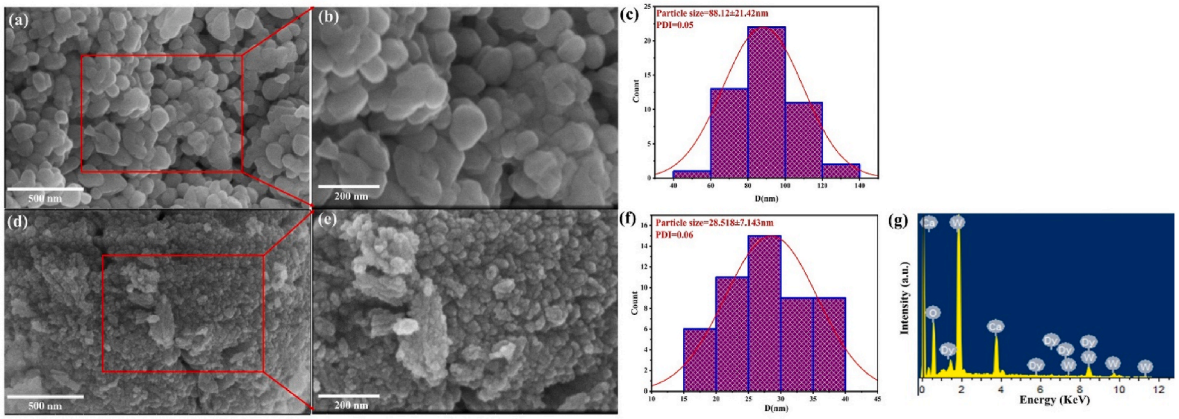


**Fig. 3.** (a–b) SEM images of $CaWO_4$, (c) Statistical size distribution histogram of $CaWO_4$, (d–e) SEM micrographs of Dy (0.8%) doped $CaWO_4$, (f) Size distribution of Dy (0.8%) doped $CaWO_4$ nanomaterials. (g) EDS spectrum of Dy (0.8%) doped $CaWO_4$ nanomaterials.

tungstate nanomaterials. The cyclic voltammograms for $CaWO_4$ and Dy (0.8%) doped $CaWO_4$ are shown in Fig. 6a and b, with sweep rates ranging from 5 to 50 mV/s and optimum potential window range from −0.1 to 0.5 V. CV profiles portray the anodic and cathodic peaks of $CaWO_4$ and Dy (0.8%) doped $CaWO_4$ corresponding to the oxidation and reduction response respectively. In the case of $CaWO_4$, the reduction doublet is positioned at 0.23 V and 0.31 V. The multiple redox peaks represent the cluster of redox activities of involved identical or distinct elements present in the solution at the surface of the electrode. It means that different oxidation states of the elements involved such as calcium (+2) and dysprosium (+3) in the electrochemical reaction [53]. The symmetric cyclic voltammogram of Dy (0.8%) doped $CaWO_4$ illustrates the reversibility of the redox reactions, revealing the charging and discharging behavior. The peak current shifts horizontally and vertically with increasing sweep rates. An increase in sweep rates offers more energy to electrolyte ions to speed up the redox processes. As a consequence, the flow of electrons and ions contacting on the surface of the electrode is significantly augmented at fast sweep rates, whereas at slow sweep rates, it is substantially lower. The peak shifting at higher sweep rates is a result of the rapid motion of charges due to the lack of sufficient time to react. The Dy (0.8%) doped calcium tungstate exhibits a significantly high value of peak current than the calcium tungstate, indicating an enhanced electrochemical response. The charge storage capacity is evaluated by the area of the CV curves and can be seen in Fig. 6c. The CV curves of Dy-doped material exhibit a considerably large area than the undoped confirming the improved specific capacity of Dy (0.8%) doped $CaWO_4$ [54]. The specific capacity ($Q_s$) is calculated by using equation (1)

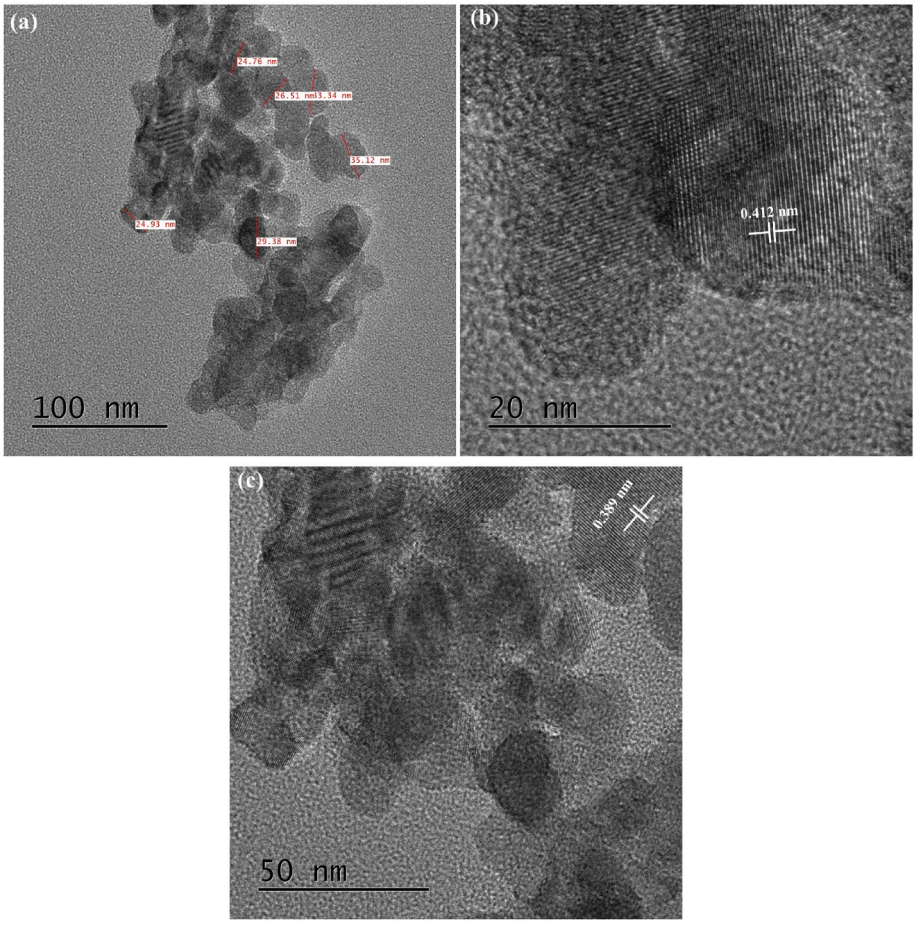


**Fig. 4.** TEM analysis of Dy (0.8%) doped CaWO4 nanomaterials; (a) low magnification image, (b–c) high resolution images showing different fringe distances.

$$Q_s = \frac{\int_{vi}^{vf} I \times VdV}{m \times \nu} \quad (1)$$

Where $\int_{vi}^{vf} I \times VdV$ = area under the CV curve, m is the active mass (g), and $\nu$ = sweep rate (mV/s). Fig. 6d displays the specific capacity trend for the fabricated $CaWO_4$ and Dy (0.8%) doped $CaWO_4$ electrodes for different sweep rates. Fig. 6d shows that the specific capacity decreases at fast sweep rates, indicating rapid kinetics [55]. At 5 mV/s, the Dy (0.8%) doped $CaWO_4$ depicts the dominant value of specific capacity (624 C/g) whereas, $CaWO_4$, has a specific capacity of 115 C/g at the same sweep rate. The CV analysis shows that Dy (0.8%) doped $CaWO_4$ modified electrode offers an enhanced electrochemical response as compared to undoped $CaWO_4$.

The estimation of the redox contributions is accomplished by using the Randles-Sevick plot. The linear relationship between sweep rate and current is estimated and the findings are shown as a Randles-Sevick plot (Fig. 7a). The slope values are calculated for oxidation (3.8892) and reduction (−3.6813) currents from a linearly fitted Randles-Sevick plot. The linear slope confirms the identical oxidation and reduction process with different sweep rates [56]. The $R^2$ values for anodic and cathodic peaks show identical behavior for oxidation and reduction, continuing the excellent reversibility and stability of the material.

The charge storage nature of fabricated electrodes is also identified by the theoretical aspect. The powers law (equations (2)–(4)), which illustrates the relation between sweep rate and current, has been applied.

$$I = a\,\nu^b \quad (2)$$

$$\log(I) = \log(a) + b\,\log(\nu) \quad (3)$$

$$\frac{\log(I)}{\log(\nu)} = b + \log(a) \quad (4)$$

Where a, b = constants, I = oxidation or reduction peak current, $\nu$ = sweep rate

According to the principle, log(I) v/s log ($\nu$) plot symbolizes the value of b. The value of b varies from 0.5 to 1, where 0.5 represents pure battery-grade material (diffusion-controlled process) and 1 indicates complete capacitive nature (surface-controlled process). Fig. 7b shows a linear trend in the plot of log (Ip) v/s log ($\nu$), with a b value of 0.61, significantly close to the theoretical assumption to reveal a diffusion-controlled process. The b values are also extracted at various fixed potentials (0.20–0.44 V) (Fig. 7c). The b values are observed in the range from 0.58 to 0.78, confirming both diffusive and surface-controlled processes as reported by Iqbal et al. (2022) [54,57].

Dunn's model is used to determine the quantitative contribution of the diffusive and surface-controlled processes. Equation (5) is given below

$$Ip(V) = K_1\nu + K_2\nu^{\sqrt{2}} \quad (5)$$

equation (5) can be modified further to equation 6

$$Ip(V) \Big/ \nu^{\sqrt{2}} = K_1\nu^{\sqrt{2}} + K_2 \quad (6)$$

The surface current is represented by the first part ($K_1\,\nu$) of equation

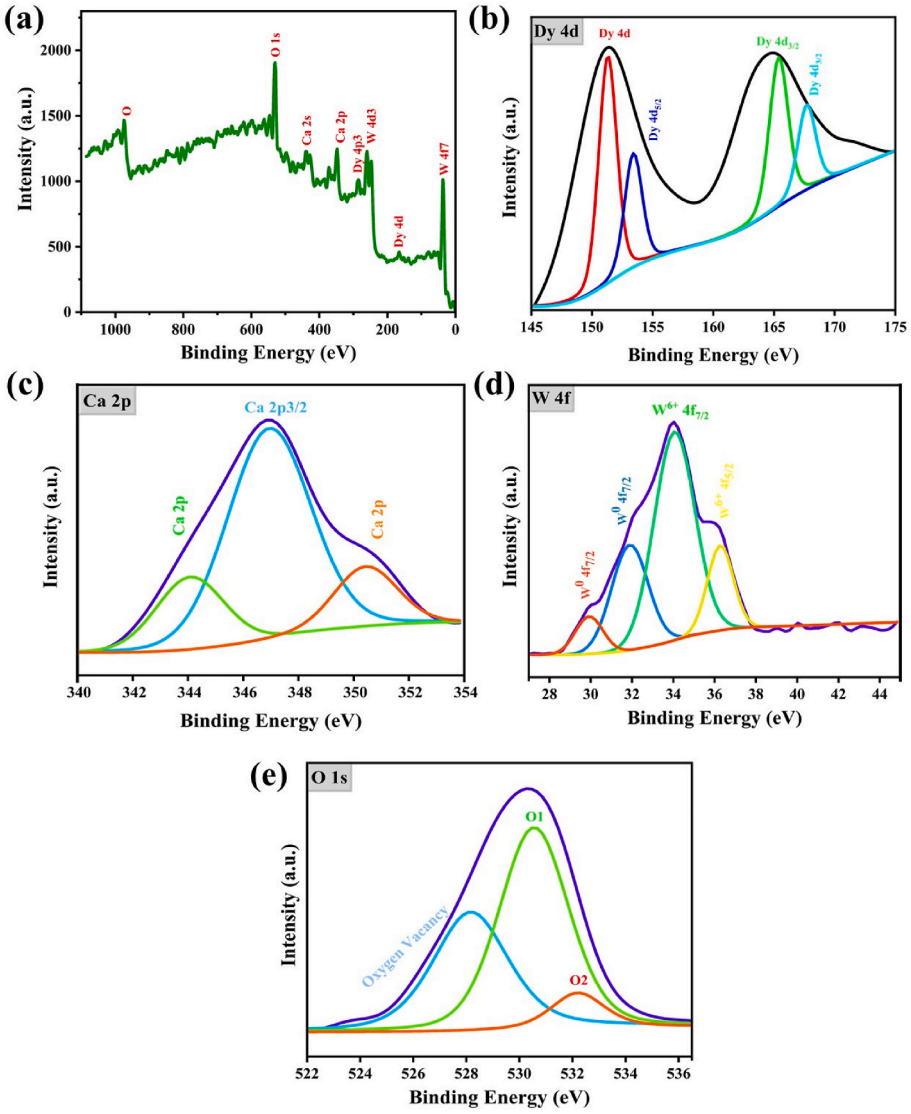


**Fig. 5.** XPS analysis of Dy (0.8%) doped $CaWO_4$ nanomaterials; (a) Survey spectrum. High-resolution spectra of (b) Dy 4d, (c) Ca 2p, (d) W 4f, (e) O 1s.

(5), while the diffusive current is represented by the second term ($K_2 \nu^{\sqrt{2}}$). Fig. 8 displays the percentage contribution of surface-controlled and diffusion-controlled processes at different sweep rates determined by using equation (6). The bar chart demonstrates that at lower sweep rates diffusion portion is dominating because the ions have sufficient time to react. The particles are unable to engage with the electrode for a longer duration at higher sweep rates due to the lack of reaction time [54]. Fig. 8 illustrates that as the sweep rate increases, the surface-controlled mechanism rises and dictates the electrochemical reaction, whereas the diffusion-controlled process diminishes. The Dy (0.8%) doped $CaWO_4$ exhibits a 63% diffusion while a 37% surface-controlled contribution at a scan rate of 50 mV/s. These outcomes reveal that Dy (0.8%) doped $CaWO_4$ appears to be a novel material for supercapattery application in the future and doping of Dy can improve the electrochemical performance of the hybrid device.

The galvanostatic charging-discharging (GCD) has been further used to investigate the electrochemical behavior of fabricated electrodes. The GCD tests are conducted at current densities of 10, 20, 30, and 50 A/g at a fixed potential of 0.5 V. Fig. 9a and b represent the GCD curves of $CaWO_4$ and Dy (0.8%) doped $CaWO_4$ modified electrodes respectively. The obtained GCD patterns have a non-linear appearance for both electrodes. The hump in the middle of the discharge curve shows the redox-active nature of the material [58]. The discharging time continues to decrease as the current density increases (Fig. 9a & b)). When the current density is at its lowest, the hydroxyl ions have a longer time to incorporate, resulting in high capacity and longer discharge times [52]. Additionally, equation (7) has been utilized to compute the specific capacity of fabricated electrodes using the parameters from GCD measurements.

$$Q_s = \frac{I \times \Delta t}{m} \tag{7}$$

Where, m, I, and Δt, symbolize the deposited mass, current, and discharging time respectively. The calculated specific capacity for $CaWO_4$ and Dy (0.8%) doped $CaWO_4$ at 10, 20, 30, and 50 A/g current densities are displayed in (Fig. 9c). The decline in the specific capacity trend is due to the slower rate of intercalation on the electrolyte/electrode interface at higher current densities [58,59]. The Dy (0.8%) doped $CaWO_4$ electrode exhibits excellent electrochemical behavior with a specific capacity of 396 C/g at a current density of 10 A/g. The addition of dysprosium in $CaWO_4$ enhances its conductivity and reduces the charge transfer resistance. Consequently, it has been proven that dysprosium-doped calcium tungstate can be an important electrode material for energy storage devices. The obtained specific capacity is found to be significantly higher as compared to other related materials (Table 2).

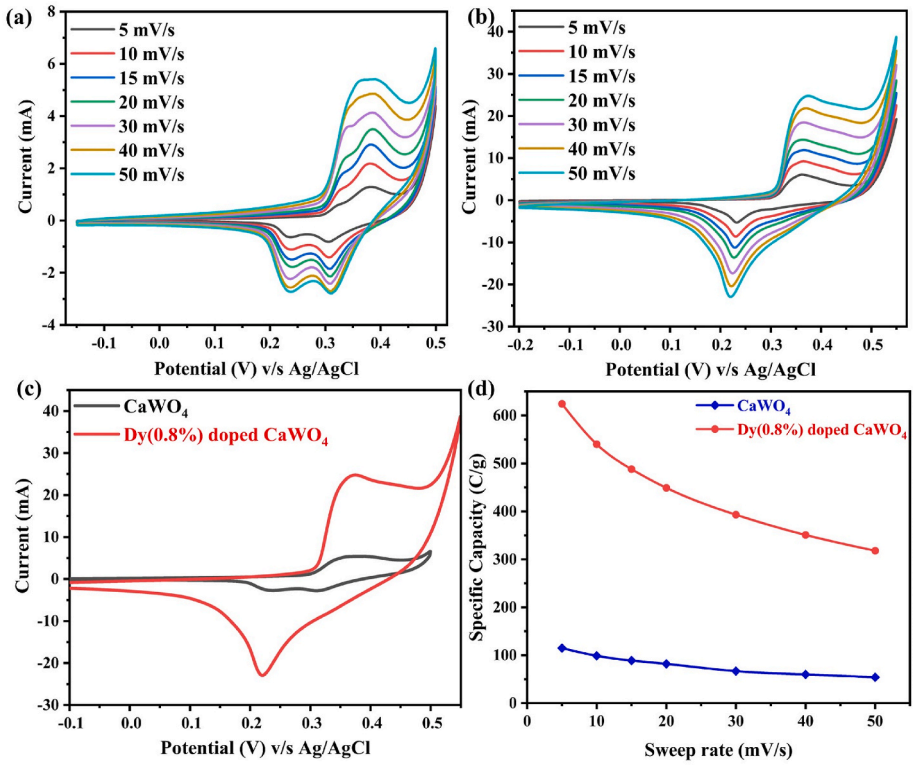


**Fig. 6.** (a) Cyclic Voltammograms of $CaWO_4$, (b) Dy (0.8%) doped $CaWO_4$ at 5 mV/s to 50 mV/s sweep rates, (c) Comparison of CV curves at 50 mV/s sweep rate (d) Specific capacitance values at different sweep rates.

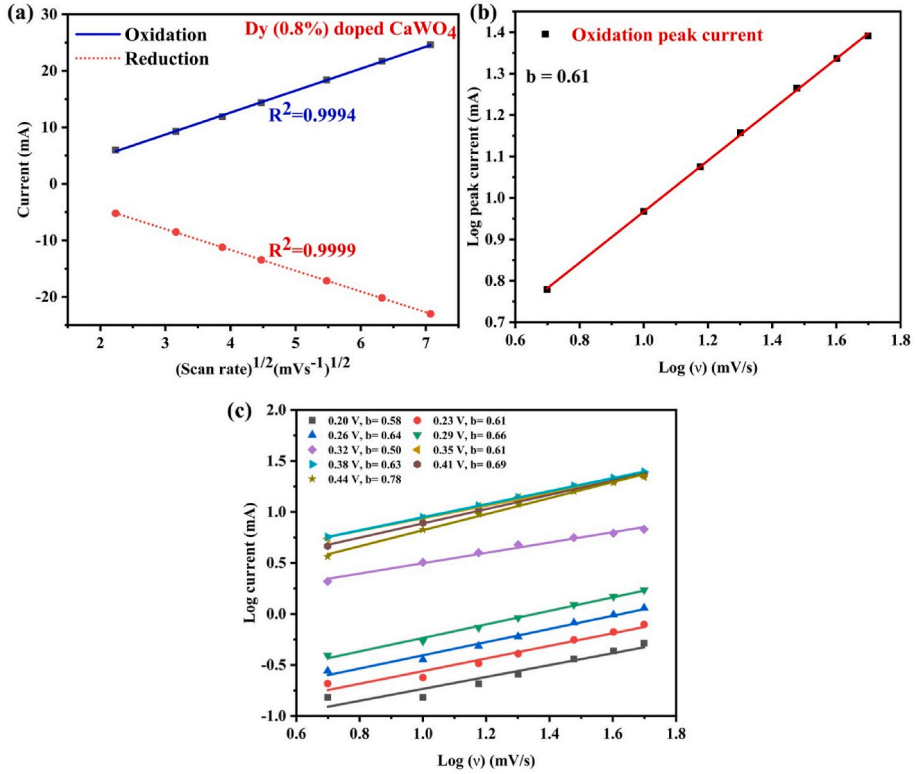


**Fig. 7.** (a) Rendles-Sevick plot of Dy (0.8%) doped $CaWO_4$ for oxidation and reduction peaks, (b) Plot of log (Ip) v/s log ($\nu$) for determining the b value, (c) Plot of log (I) v/s log ($\nu$) at different fixed potentials for obtaining the values of b.

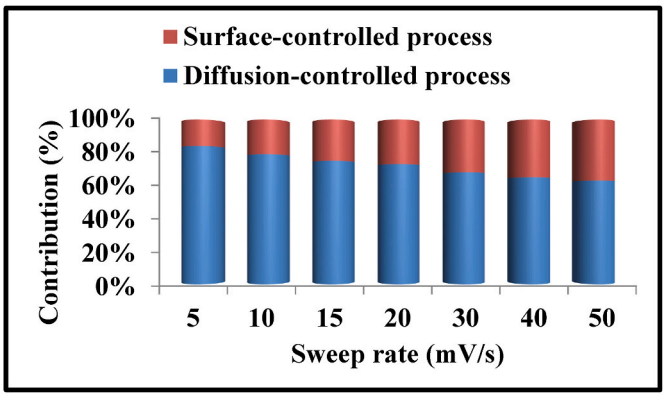


**Fig. 8.** Percentage contribution of surface-controlled and diffusive-controlled processes at different sweep rates.

The electrochemical impedance spectroscopy (EIS) technique is employed to investigate electron transfer at the electrode interface [52]. In EIS, the electrode impedance is determined based on the frequency ranges from 0.3 Hz to 100 kHz at a fixed potential of 10 mV [62]. The Nyquist plots for $CaWO_4$ and Dy (0.8%) doped $CaWO_4$ electrodes are obtained to display the behavior of the imaginary impedance and the real impedance. The Nyquist plot reveals the essential details: equivalent series resistance (ESR) refers to the resistance that accumulates during a chemical process at the electrolyte and electrode contact can be estimated by the x-intercept at the higher frequency, whereas the semi-circle in the high-frequency region represents the charge transfer resistance (Rct). The accretion of OH ions provides a straight line at the low-frequency domain to investigate the Warburg impedance (W) [55, 57–59]. It is believed that $Dy^{3+}$ can create more oxygen vacancies due to higher charge as compare to $Ca^{2+}$. This formation of vacancies can increase the electrical conductivity which develop higher current in CV graph and lesser Rct [31]. On the other hand, W remains intact during the electrochemical reaction, however, enhances the conducting channels for electrolytic ions which increases specific capacity [3]. This caused easy access of electrolyte ions transport from KOH solution to the nanomaterial's surface. provides stability. The comparative EIS spectrums of undoped $CaWO_4$ and Dy doped $CaWO_4$ electrodes are portrayed in Fig. 10a whereas the high-frequency region is displayed in the inset. At the high-frequency region, the $R_{ct}$ values for $CaWO_4$ and Dy (0.8%) doped $CaWO_4$ electrodes have been determined to be 15 Ω and 12 Ω respectively. The Dy(0.8%) doped $CaWO_4$ electrode exhibits smaller charge transfer resistance which demonstrates enriched redox reactions and higher electrical conductivity of Dy (0.8%) doped $CaWO_4$ [55]. The EIS tests reveal promising ionic conductivity. The equivalent circuit modeling was also performed (Fig. 10b). The equivalent circuit R(QR)(CR)(CR)) is shown in Fig. 10b (inset) and consists of three staircases parallel R–C circuit. The components of the equivalent circuit symbolize the solution resistance (Rs) of activated electrode and KOH electrolyte, constant phase element (Q), charge transfer resistance (Rct) between electrode/electrolyte interface. The high frequency R1-C1 circuit represents resistance and capacitance of nanomaterials' surface whereas medium range R2-C2 circuit corresponds to double layer capacitance and charge transfer resistance [63–65].

## 4. Conclusion

In summary, facile hydrothermal method was employed for the fabrication of $CaWO_4$ and dysprosium-doped $CaWO_4$ nanomaterials with different concentrations (0.4%, 0.6%, 0.8%). The XRD, SEM, EDX,

**Table 2**
A comparison between the present study and previously reported work.

| Sample name | Specific capacity/ capacitance | Current density | Refs. |
|---|---|---|---|
| **α-$MnO_2$: Dy (15%)** | 100 F/g | 0.1 A/g | [30] |
| **$Li_{4-x/3}Ti_{5-2x/3}Dy_xO_{12}$ (x = 0.02)** | 181.8 mAh g | 20 C | [60] |
| **Dy-IONPs** | 202 F/g | 0.5 A/g | [29] |
| **MnWO4** | 219 F/g | 0.4 A/g | [61] |
| **Dy (0.8%) doped $CaWO_4$** | 396 C/g | 10 A/g | Present study |

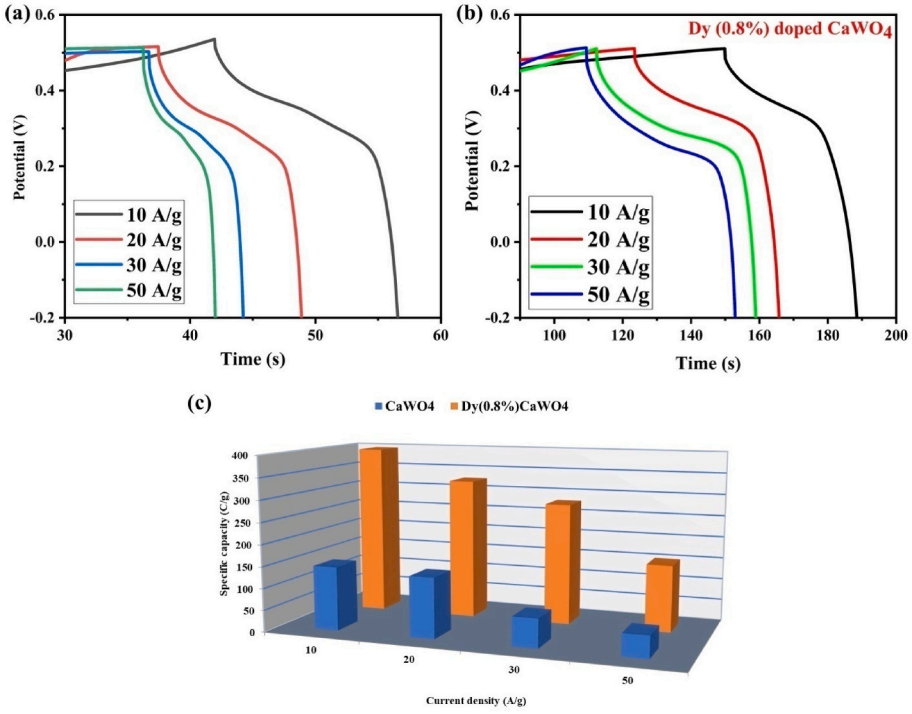


**Fig. 9.** (a) GCD profiles of $CaWO_4$ (b) GCD profiles of Dy (0.8%) doped $CaWO_4$ at different current densities (c) Specific capacity variation for current density.

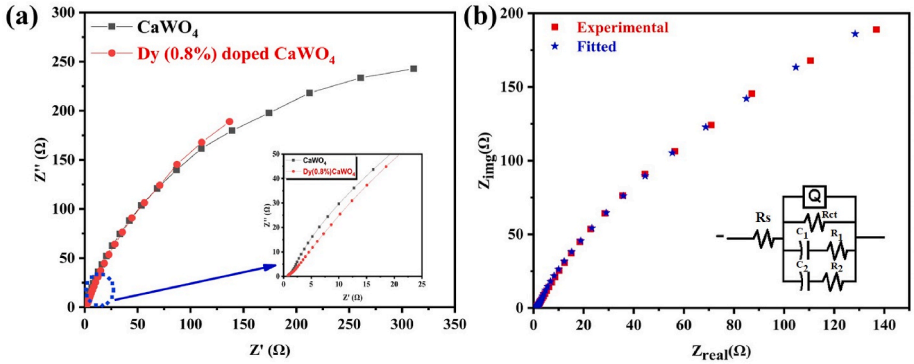


**Fig. 10.** Nyquist plot: (a) Comparative EIS spectrums of undoped and Dy doped $CaWO_4$electrode, (b) Fitting on Dy (0.8%) doped $CaWO_4$ EIS spectrum. (Inset) Equivalent circuit modeling.

FTIR, XPS, and UV–Vis spectroscopy were utilized for the characterization of nanomaterials. The electrochemical studies showed that the electrochemical performance of $CaWO_4$ was considerably improved with Dy addition. The GCD of prepared Dy (0.8%) doped $CaWO_4$-based electrode shows the highest specific capacity of 396 C/g than 146 C/g of $CaWO_4$ at 10 A $g^{-1}$ current density. The CV curves show that surface-controlled mechanism increases with the scan rate. There is a 37% surface-controlled process and 63% diffusion-controlled mechanism at a scan rate of 50 mV/s. This outcome makes it a unique material for supercapattery applications in the future.

## Declaration of competing interest

The authors declare that they have no known competing financial interests or personal relationships that could have appeared to influence the work reported in this paper.

## Acknowledgments

The authors would like to acknowledge the financial assistance from the Higher Education Commission (HEC) of Pakistan, for providing funds under NRPU Research Project No: 7487/Punjab/NRPU/R&D/HEC/2017.

## References

[1] S. Swathi, R. Yuvakkumar, P.S. Kumar, G. Ravi, D. Velauthapillai, Hexamethylenetetramine concentration effect on CaWO4 for electrochemical hydrogen evolution reaction activity, Fuel 306 (2021), 121781.
[2] A. González, E. Goikolea, J.A. Barrena, R. Mysyk, Review on supercapacitors: technologies and materials, Renew. Sustain. Energy Rev. 58 (2016) 1189–1206.
[3] M.R. Khawar, N.A. Shad, S. Hussain, Y. Javed, M.M. Sajid, A. Jilani, M. Faheem, A. Asghar, Cerium oxide nanosheets-based tertiary composites (CeO2/ZnO/ZnWO4) for supercapattery application and evaluation of faradic & non-faradic capacitive distribution by using Donn's model, J. Energy Storage 55 (2022), 105778.
[4] W. Yang, M. Ni, X. Ren, Y. Tian, N. Li, Y. Su, X. Zhang, Graphene in supercapacitor applications, Curr. Opin. Colloid Interface Sci. 20 (5–6) (2015) 416–428.
[5] S. Karthikeyan, B. Narenthiran, A. Sivanantham, L.D. Bhatlu, T. Maridurai, Supercapacitor: evolution and review, Mater. Today Proc. 46 (2021) 3984–3988.
[6] Y. Wang, X. Wu, Y. Han, T. Li, Flexible supercapacitor: overview and outlooks, J. Energy Storage 42 (2021), 103053.
[7] R. Lakra, R. Kumar, P.K. Sahoo, D. Thatoi, A. Soam, A mini-review: graphene based composites for supercapacitor application, Inorg. Chem. Commun. 133 (2021), 108929.
[8] V.V. Mohan, P. Anjana, R. Rakhi, A study on the effect of phase conversion of tungsten nanostructures on their electrochemical energy storage performance, Mater. Adv. 3 (14) (2022) 5900–5910.
[9] P. Bagwade, D. Malavekar, T. Ghogare, S. Ubale, V. Mane, R. Bulakhe, I. In, C. Lokhande, A high performance flexible solid-state asymmetric supercapacitor based on composite of reduced graphene oxide@ dysprosium sulfide nanosheets and manganese oxide nanospheres, J. Alloys Comp. 859 (2021), 157829.
[10] Z. Bi, X. Li, Y. Chen, X. He, X. Xu, X. Gao, Large-scale multifunctional electrochromic-energy storage device based on tungsten trioxide monohydrate nanosheets and prussian white, ACS Appl. Mater. Interfaces 9 (35) (2017) 29872–29880.
[11] U. García-Pérez, A. Martinez-de La Cruz, J. Peral, Transition metal tungstates synthesized by co-precipitation method: basic photocatalytic properties, Electrochim. Acta 81 (2012) 227–232.
[12] A. Sobhani-Nasab, M. Rahimi-Nasrabadi, H.R. Naderi, V. Pourmohamadian, F. Ahmadi, M.R. Ganjali, H. Ehrlich, Sonochemical synthesis of terbium tungstate for developing high power supercapacitors with enhanced energy densities, Ultrasonics sonochem. 45 (2018) 189–196.
[13] D. Errandonea, F.J. Manjon, Pressure effects on the structural and electronic properties of ABX4 scintillating crystals, Prog. Mater. Sci. 53 (4) (2008) 711–773.
[14] H. Gao, S. Wang, Y. Wang, H. Yang, F. Wang, S. Tang, Z. Yi, D. Li, CaMoO4/CaWO4 heterojunction micro/nanocomposites with interface defects for enhanced photocatalytic activity, Colloids Surf., A 642 (2022), 128642.
[15] T. Thongtem, S. Kungwankunakorn, B. Kuntalue, A. Phuruangrat, S. Thongtem, Luminescence and absorbance of highly crystalline CaMoO4, SrMoO4, CaWO4 and SrWO4 nanoparticles synthesized by co-precipitation method at room temperature, J. Alloys Comp. 506 (1) (2010) 475–481.
[16] M. Erdoğan, İ. Karakaya, On the electrochemical reduction mechanism of CaWO4 to W powder, Metall. Mater. Trans. B 43 (4) (2012) 667–670.
[17] N.A. Sabu, X. Francis, J. Anjaly, S. Sankararaman, T. Varghese, Enhanced structural and optical properties of the polyaniline-calcium tungstate (PANI-CaWO4 nanocomposite for electronics applications, Eur. Phys. J. Plus 132 (6) (2017) 1–7.
[18] A. Sobhani-Nasab, M. Sadeghi, Preparation and characterization of calcium tungstate nanoparticles with the aid of amino acids and investigation its photocatalytic application, J. Mater. Sci. Mater. Electron. 27 (8) (2016) 7933–7938.
[19] S. Arora, B. Chudasama, *Crystallization and optical properties of CaWO4 and SrWO4.* Crystal Research and Technology, J. Exper. Indust. Crystall. 41 (11) (2006) 1089–1095.
[20] H. Wu, J. Peng, H. Sun, Q. Ruan, H. Dong, Y. Jin, Z. Sun, Y. Hu, Surface activation of calcium tungstate by europium doping for improving photocatalytic performance: towards lanthanide site photocatalysis, Chem. Eng. J. 432 (2022), 134339.
[21] F. Zhu, Z. Xiao, L. Yan, F. Zhang, A. Huang, The influence on intrinsic light emission of calcium tungstate and molybdate powders by multivalence Pr codoping, Appl. Phys. A 101 (4) (2010) 689–693.
[22] S. Deng, W. Zhang, Z.-F. Hu, Z.-Y. Feng, L. Ma, Y.-M. Pan, X. Sheng, L. Luo, Photoluminescence and photocatalytic activity in Ca2+ and Dy3+ Co-doped ZnWO4 system, in: Proceeding of 2017 Joint International Conference on Materials Science and Engineering Application (ICMSEA 2017) and International Conference on Mechanics, Civil Engineering and Building Materials, MCEBM, 2017, 2017.
[23] S. Wang, H. Gao, G. Sun, Y. Li, Y. Wang, H. Liu, C. Chen, Y. Liang, Structure characterization, optical and photoluminescence properties of scheelite-type CaWO4 nanophosphors: effects of calcination temperature and carbon skeleton, Opt. Mater. 99 (2020), 109562.
[24] Y.-M. Zhang, H.-P. Huang, X. Liang, A novel electrochemical sensor based on Au-Dy2 (WO4) 3 nanocomposites for simultaneous determination of uric acid and nitrite, Chin. J. Anal. Chem. 48 (3) (2020) e20032–e20037.
[25] A. Raja, K. Selvakumar, M. Swaminathan, M. Kang, Redox additive based rGO-Dy2WO6-ZnO nanocomposite for enhanced electrochemical supercapacitor applications, Synth. Met. 276 (2021), 116753.
[26] C. Yan, X. Yang, H. Zhao, H. Zhong, G. Ma, Y. Qi, B.E. Koel, Y. Ju, Controlled Dy-doping to nickel-rich cathode materials in high temperature aerosol synthesis, Proc. Combust. Inst. 38 (4) (2021) 6623–6630.
[27] P. Kaur, A. Khanna, M. Singh, A. Sinha, Structural and optical characterization of Eu and Dy doped CaWO4 nanoparticles for white light emission, J. Alloys Comp. 834 (2020), 154804.
[28] A. Khanna, P.S. Dutta, CaWO4: Eu3+, Dy3+, Tb3+ phosphor crystals for solid-state lighting applications, ECS Trans. 41 (37) (2012) 39.
[29] M. Aghazadeh, M.R. Ganjali, Evaluation of supercapacitive and magnetic properties of Fe3O4 nano-particles electrochemically doped with dysprosium cations: development of a novel iron-based electrode, Ceram. Int. 44 (1) (2018) 520–529.

[30] D. Gangwar, P. Tiwari, A. Kumar, R. Prakash, C. Rath, Effect of Dy on electrochemical supercapacitive behaviour of α-MnO2 nanorods, Electrochim. Acta 328 (2019), 135027.
[31] D. Alhashmialameer, S. Aman, M. Abdullah, R.Y. Khosa, S. Manzor, H.M. Ali, M. H. Helal, H.M.T. Farid, M.S. Waheed, T.A. Taha, Facile hydrothermal synthesis of Dy-doped NiMnO3 nanoflakes as a highly stable electrode for energy conversion system, J. Sol. Gel Sci. Technol. 105 (1) (2023) 85–97.
[32] L. Grandell, A. Lehtilä, M. Kivinen, T. Koljonen, S. Kihlman, L.S. Lauri, Role of critical metals in the future markets of clean energy technologies, Renew. Energy 95 (2016) 53–62.
[33] A. Phuruangrat, T. Thongtem, S. Thongtem, Synthesis, characterisation and photoluminescence of nanocrystalline calcium tungstate, J. Exp. Nanosci. 5 (3) (2010) 263–270.
[34] W. Wang, P. Yang, S. Gai, N. Niu, F. He, J. Lin, Fabrication and luminescent properties of CaWO4: Ln3+ (Ln= Eu, Sm, Dy) nanocrystals, J. Nanoparticle Res. 12 (6) (2010) 2295–2305.
[35] M. Sadegh, A. Badiei, A. Abbasi, H. Goldooz, G.M. Ziarani, Preparation of CaWO4: Ln3+@ SiO2 (Ln= Tb, Dy and Ho) nanoparticles by a combustion reaction and their optical properties, J. Lumin. 130 (11) (2010) 2072–2075.
[36] P. Du, L.K. Bharat, X.-Y. Guan, J.S. Yu, Synthesis and luminescence properties of color-tunable Dy3+-activated CaWO4 phosphors, J. Appl. Phys. 117 (8) (2015), 083112.
[37] H. Miao, M. Dong, G. Tan, Y. Pu, Doping effects of Dy and Mg on BaTiO3 ceramics prepared by hydrothermal method, J. Electroceram. 16 (4) (2006) 297–300.
[38] R. Mohadi, A. Sueb, K. Anggraini, A. Lesbani, Calcium oxide catalyst based on quail eggshell for biodiesel synthesis from waste palm oil, J. Pure Appl. Chem. Res. 7 (2) (2018) 130.
[39] S.L. Ortiz, V.R. Lugo, D. Salado-Leza, M. Reyes-Valderrama, L. Alcántara-Quintana, P. González-Martínez, D.M. Anaya, Dy2O3-unpurified hydroxyapatite: a promising thermoluminescent sensor and biomimetic nanotherapeutic, Appl. Phys. A 127 (12) (2021) 1–13.
[40] S. Wang, H. Gao, Y. Jin, X. Chen, F. Wang, H. Yang, L. Fang, S. Tang, D. Li, Defect engineering in novel broad-band gap hexaaluminate MAl12O19 (M= Ca, sr, Ba)-Based photocatalysts Boosts Near ultraviolet and visible light-driven photocatalytic performance, Mater. Today Chem. 24 (2022), 100942.
[41] S. Wang, M. Li, H. Gao, Z. Yin, C. Chen, H. Yang, L. Fang, V.J. Angadi, Z. Yi, D. Li, Construction of CeO2/YMnO3 and CeO2/MgAl2O4/YMnO3 photocatalysts and adsorption of dyes and photocatalytic oxidation of antibiotics: performance prediction, degradation pathway and mechanism insight, Appl. Surf. Sci. 608 (2023), 154977.
[42] A.A. Radhakrishnan, B.B. Beena, Structural and optical absorption analysis of CuO nanoparticles, Indian J. Adv. Chem. Sci. 2 (2) (2014) 158–161.
[43] F.X. Nobre, I.C. Nogueira, G.d.S. Souza, J.M.E.d. Matos, P.R.r.d.C. Couceiro, W. R. Brito, J.P.r. de la Cruz, Y. Leyet Ruiz, Structural and optical properties of Ca0. 9Cu0. 01WO4 solid solution synthesized by sonochemistry method at room temperature, Inorg. Chem. 59 (9) (2020) 6039–6046.
[44] D. Sivaganesh, S. Saravanakumar, V. Sivakumar, R. Rajajeyaganthan, M. Arunpandian, J.N. Gopal, T. Thirumalaisamy, Surfactants-assisted synthesis of ZnWO4 nanostructures: a view on photocatalysis, photoluminescence and electron density distribution analysis, Mater. Char. 159 (2020), 110035.
[45] B. Grobelna, A. Synak, D. Głowaty, P. Bojarski, E. Szczepańska, K. Szczodrowski, I. Gryczynski, J. Karczewski, Novel inorganic xerogels doped with CaWO4: xDy: synthesis, characterization and luminescence properties, Mater. Chem. Phys. 199 (2017) 166–172.
[46] D. Barreca, A. Gasparotto, A. Milanov, E. Tondello, A. Devi, R.A. Fischer, Nanostructured Dy2O3 films: an XPS investigation, Surf. Sci. Spectra 14 (1) (2007) 52–59.
[47] T. Akitsu, Y. Einaga, Structures and XPS studies of several 3d–4f cyano-bridged LnIII–FeIII/CoIII heterometallic complexes, Polyhedron 25 (13) (2006) 2655–2662.
[48] F. Voigts, F. Bebensee, S. Dahle, K. Volgmann, W. Maus-Friedrichs, The adsorption of CO2 and CO on Ca and CaO films studied with MIES, UPS and XPS, Surf. Sci. 603 (1) (2009) 40–49.
[49] B. Demri, D. Muster, XPS study of some calcium compounds, J. Mater. Process. Technol. 55 (3–4) (1995) 311–314.
[50] W.-L. Dai, M.-H. Qiao, J.-F. Deng, XPS studies on a novel amorphous Ni–Co–W–B alloy powder, Appl. Surf. Sci. 120 (1–2) (1997) 119–124.
[51] Z. Urgessa, C. Mbulanga, S.T. Djiokap, J. Botha, M. Duvenhage, H. Swart, The defect passivation effect of hydrogen on the optical properties of solution-grown ZnO nanorods, Phys. B Condens. Matter 480 (2016) 48–52.
[52] Z. Maliha, M. Rani, R. Neffati, A. Mahmood, M.Z. Iqbal, A. Shah, Investigation of copper/cobalt MOFs nanocomposite as an electrode material in supercapacitors, Int. J. Energy Res. 46 (12) (2022) 17404–17415.
[53] N. Elgrishi, K.J. Rountree, B.D. McCarthy, E.S. Rountree, T.T. Eisenhart, J. L. Dempsey, A practical beginner's guide to cyclic voltammetry, J Chem. Educ. 95 (2) (2018) 197–206.
[54] M.Z. Iqbal, S. Siddique, M. Shaheen, S. Alam, M. Alzaid, Role of Ag and Cu as an interfacial layer on the electrochemical performance of Ni/Ag/Co3(PO4)2 and Ni/Cu/Co3(PO4)2 electrodes for hybrid energy storage devices, Ceram. Int. 48 (11) (2022) 15686–15694.
[55] M.Z. Iqbal, U. Abbasi, M. Alzaid, Cobalt manganese phosphate and sulfide electrode materials for potential applications of battery-supercapacitor hybrid devices, J. Energy Storage 50 (2022), 104632.
[56] S.E. Arasi, R. Ranjithkumar, P. Devendran, M. Krishnakumar, A. Arivarasan, Studies on electrochemical mechanism of nanostructured cobalt vanadate electrode material for pseudocapacitors, J. Energy Storage 41 (2021), 102986.
[57] M.Z. Iqbal, M.M. Faisal, S.R. Ali, A.M. Afzal, M.R. Abdul Karim, M.A. Kamran, T. Alharbi, Strontium phosphide-polyaniline composites for high performance supercapattery devices, Ceram. Int. 46 (8) (2020) 10203–10214. Part A).
[58] S.S. Haider, S. Dad, S. Zakar, M.Z. Iqbal, Mechanistic scrutinizing the charge storage phenomena of battery-grade Mn-Co-S electrodes, Mater. Res. Bull. 156 (2022), 111953.
[59] S.S. Haider, S. Zakar, M. Zahir Iqbal, S. Dad, Battery-type electrodeposited ternary metal sulfides electrodes for advanced hybrid energy storage devices, J. Electroanal. Chem. 904 (2022), 115881.
[60] Y. Cai, Y. Huang, W. Jia, Y. Zhang, X. Wang, Y. Guo, D. Jia, W. Pang, Z. Guo, L. Wang, Two-dimensional dysprosium-modified bamboo-slip-like lithium titanate with high-rate capability and long cycle life for lithium-ion batteries, J. Mater. Chem. 4 (45) (2016) 17782–17790.
[61] F. Li, X. Xu, J. Huo, W. Wang, A simple synthesis of MnWO4 nanoparticles as a novel energy storage material, Mater. Chem. Phys. 167 (2015) 22–27.
[62] A. Noori, M.F. El-Kady, M.S. Rahmanifar, R.B. Kaner, M.F. Mousavi, Towards establishing standard performance metrics for batteries, supercapacitors and beyond, Chem. Soc. Rev. 48 (5) (2019) 1272–1341.
[63] R. He, Y. Gao, M. Yan, L. Zhang, Z. Liu, Electrochemical impedance spectroscopy study of copper corrosion inhibition by PASP in 3% citric acid, Desalination Water Treat. 175 (2020) 189–195.
[64] M. Ates, F. Arican, T. Karazehir, Electrochemical copolymerization of N-methylpyrrole and 2, 2′-bithitiophene; characterization, micro-capacitor study, and equivalent circuit model evaluation, Bull. Mater. Sci. 36 (7) (2013) 1281–1290.
[65] M. Ates, N. Uludag, Capacitive behaviors and monomer concentration effects of poly (9-benzyl-9H-carbazole) on carbon fiber microelectrode, Fiber. Poly. 12 (3) (2011) 296–302.